

pubs.acs.org/acsapm Article

# Electrically Conductive Kevlar Fibers and Polymer-Matrix Composites Enabled by Atomic Layer Deposition

Robin E. Rodríguez, Tae Hwa Lee, Yuxin Chen, Eric Kazyak, Claire Huang, Tae H. Cho, William S. LePage, M. D. Thouless, Mihaela Banu, and Neil P. Dasgupta\*



Cite This: ACS Appl. Polym. Mater. 2021, 3, 5959–5968



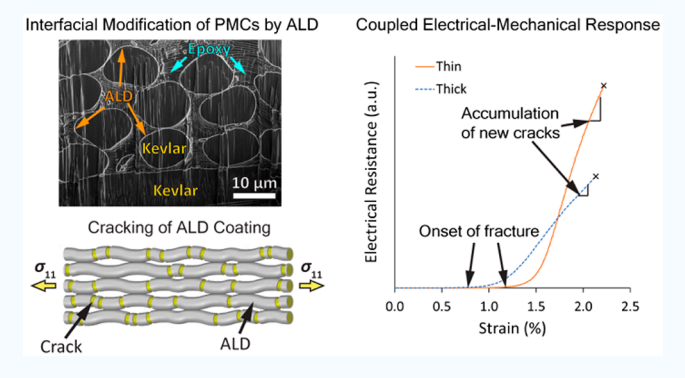
ACCESS

Metrics & More

Article Recommendations

Supporting Information

ABSTRACT: Multifunctional composites that incorporate non-structural capabilities such as energy storage, self-healing, and structural health monitoring have the potential to transform load-bearing components in automotive and aerospace vehicles. Imparting electrical conductivity into polymer-matrix composites (PMCs) is an important step in enabling multifunctionality while maintaining mechanical stiffness and strength. In this work, electrically conductive PMCs were fabricated by conformally coating Kevlar 49 woven fabrics with aluminum-doped zinc oxide using atomic layer deposition (ALD). Electrical resistance was measured at the single-fiber, single-tow, and woven fabric levels as a function of coating thickness. The ALD coatings on adjacent fibers merge as their thickness increases, resulting in an



interconnected network with improved percolation and lower resistance. After ALD, the fabrics were embedded in an epoxy matrix to manufacture PMCs. The electrical resistance of the composites increased with applied tensile strain, which was attributed to cracking of the conductive coatings. The relative change in resistance as a function of strain varied with coating thickness, which was rationalized by a thin-film fracture mechanics model. This work demonstrates a pathway for scalable and tunable incorporation of electrical conductivity into fiber-reinforced composites without significantly changing their density or load-bearing capabilities.

KEYWORDS: atomic layer deposition, composite, polymer, fiber, mechanical properties, multifunctional, fracture, electrical properties

## **■** INTRODUCTION

Fiber-reinforced composites (FRCs) are low-density materials that have been widely used as structural components in high-performance automotive and aerospace vehicles. FRCs can be designed to have a high specific strength, stiffness, and/or toughness, and their lightweight characteristics can offer significant improvements in performance and fuel efficiency. Over the past two decades, a variety of multifunctional composites have been developed, including structural batteries and supercapacitors, electromagnetic interference shielding, and self-healing materials. Imparting additional functionality to FRCs while maintaining their lightweight and structural qualities is highly desirable to save space and augment the performance of automotive and aerospace vehicles.

To enable multifunctionality in FRCs, there is a need to modify nonstructural properties such as thermal and electrical conductivity. This is often achieved through the inclusion of additives or coatings. For example, to design FRCs that also function as an electronic device, constituents with electrically conducting and semiconducting qualities are necessary. However, polymer-matrix composites (PMCs) are generally

electrically insulating, which often necessitates the inclusion of electrically conductive additives. For FRCs, reinforcements that are intrinsically conductive, such as carbon fibers, may be used. However, restricting the materials selection to intrinsically conductive fabrics may significantly limit the material design flexibility. For example, while the conductance of a carbon-fiber reinforced PMC can be increased by increasing the volume fraction of the fibers, this also impacts its density, stiffness, and strength. In composites where all constituents are electrically insulating, a common strategy to impart conductivity is to mix electrically conductive additives such as carbon black, <sup>14–16</sup> graphene, <sup>17,18</sup> or carbon nanotubes <sup>19–24</sup> into the matrix. However, such additives tend to affect the bulk mechanical properties and density of the final product, <sup>25–27</sup> which may not be desired. Furthermore, the distribution of these additives may not be uniform in composites that use

Received: September 17, 2021 Accepted: September 28, 2021 Published: October 14, 2021





braided/woven fabrics, resulting in inhomogeneous mechanical and electrical properties.<sup>20</sup> Therefore, there is a desire to decouple the electrical response of the composite from its mechanical properties, enabling improved control of materials by design.

A potential method to tune electrical conductivity without significantly affecting the stiffness, strength, and density is to modify the surface of the reinforcement with a thin, uniform, and conformal conductive coating before incorporation into the matrix. Chemical vapor deposition (CVD)<sup>28–30</sup> and electrophoretic deposition (EPD)<sup>31</sup> have been explored as methods for coating fabrics. However, many thin-film deposition methods suffer from trade-offs between conformality, uniformity, and precise thickness control at the nanoscale, especially when coating 3-D topologies with high aspect-ratios. This highlights the need for coating processes that maintain precise control and tunability of thickness and composition when coating fibers, tows, and fabrics that are used in PMCs.

Among the potential thin-film deposition techniques, atomic layer deposition (ALD) provides unparalleled conformality with subnanometer resolution in material thickness and composition, which are ideal characteristics when coating complex 3-D topologies such as woven fabrics.<sup>32–37</sup> ALD is a vapor-phase deposition technique that utilizes two or more precursors that react with the substrate in a self-limiting manner that is not line-of-sight-dependent. The precursors react in sequential steps, allowing for precise tuning of film thickness and composition. Additionally, a wide range of materials can be deposited using ALD,<sup>38</sup> including ceramics, metals, and polymers. This broad materials selection allows for the design of materials with specified properties, representing a powerful method for incorporating multifunctionality into composites.<sup>39</sup> Previous contributions have demonstrated that ALD can conformally coat fibers<sup>40–44</sup> and that they can be made to be conductive.<sup>45–48</sup> Furthermore, the effects interconnected fibers in woven<sup>49</sup> and nonwoven fabrics have on their conductive properties have been studied.<sup>50</sup> Normal compressive forces on woven and nonwoven fabrics have been shown to improve through-fabric conductance as a result of enhanced fiber-fiber contact, which minimizes contact resistance within the fiber structure.<sup>45</sup> ALD coating of fibers has shown promise for engineering the mechanical response of polymer interfaces and PMCs. 40,51,52 However, the use of ALD to impart electrical conductivity into PMCs has not been previously studied, which represents an important step toward multifunctional composites by design. Moreover, there is a need to quantify the coupled mechanical and electrical behavior of these multifunctional PMCs under applied loads in order to identify the design constraints and criteria for cooptimization of their functional and structural properties.

In this work, we use ALD to impart electrical conductivity onto Kevlar 49 (K49) woven fabrics by coating them with aluminum-doped zinc oxide (AZO). AZO was selected as the coating material because it has a low electrical resistivity  $(\sim 10^{-3}~\Omega \cdot \text{cm})^{53,54}$  and can be deposited at relatively low temperatures (<150 °C), which minimizes physical damage to the K49 fabric. The conductive properties of the coated fabrics were measured as a function of ALD film thickness at the single-fiber, single-tow, and woven fabric levels. The trends in thickness-dependent conductivity were explored with scanning electron microscopy/plasma focused-ion beam (SEM-PFIB) analysis. The coated fabrics were integrated into PMCs with an epoxy matrix using a vacuum-assisted resin-transfer-molding

(VARTM) process.<sup>55</sup> The mechanical properties of the PMCs were evaluated, and their multifunctional properties were characterized through *in situ* measurements of electrical conductivity during tensile testing. The change in electrical response with increasing strain was analyzed, which was described with a fracture mechanics model. The results of this study highlight the importance of precise thickness control and conformality in the coating of multifunctional composites and explore the role of thin-film mechanics in determining the limits of functional interlayers under applied loads.

## **EXPERIMENTAL METHODS**

K49 fabrics in a 351-style plain weave (JPS Composite Materials, Corp.) were used for this study. The single fibers, single tows, and woven fabric samples were extracted and cleaned as described in the Supporting Information. A custom-built, hot-wall, crossflow atomic layer deposition (ALD) reactor<sup>56</sup> was used. The precursors were diethylzinc (DEZ, 52 wt % Zn, Sigma-Aldrich), dimethylaluminum isopropoxide (DMAI, 98% (99.99+%-Al), Strem Chemicals, Inc.), and deionized water. The ALD reactor was heated to 130 °C, and the DMAI source was heated to 65 °C; the DEZ and water were kept at room temperature. Argon (99.999% purity) was used as the carrier gas at 70 sccm. The recipe for ALD coatings consist of repeating a sequence of precursor-A/argon/precursor-B/argon. For the ternary AZO growth, this sequence represents a "subcycle", which is integrated into a "supercycle" recipe. The ratio of ZnO:Al<sub>2</sub>O<sub>3</sub> subcycles within a supercycle determines the final Zn:Al ratio in the ALD film.<sup>54</sup> DEZ and DMAI are precursor-A for their respective subcycles and precursor-B uses DI water for both cases. The time sequence for both subcycles was 0.05 s/45 s/0.10 s/45 s. One supercycle consisted of a ratio of 15:1 DEZ:DMAI subcycles. The average growth rate of AZO on Si wafers was measured to be 29.6 Å/ supercycle or 1.9 Å/cycle using spectroscopic ellipsometry. The total number of supercycles was adjusted in each run to achieve a targeted AZO thickness between 40 and 200 nm. Scanning electron microscopy (SEM; Thermo Fisher Helios G4 PFIB UXe), X-ray photoelectron spectroscopy (XPS; Kratos Axis Ultra), and X-ray diffraction (XRD; Rigaku Smartlab) were used to confirm the composition and phase of the AZO coating on the K49 fabrics (Figures S1 and S2). After the K49 single fibers, tows, and fabrics were coated to specified thicknesses, their electrical resistance was measured with an SP-200 Biologic potentiostat using a four-point probe<sup>57</sup> (details in the Supporting Information).

Single-ply PMCs were manufactured using the VARTM method (details in the Supporting Information). The matrix polymer was a bisphenol A, low-viscosity epoxy resin (R-3501, Composite Envisions, LLC) and hardener (H-5000-01, Composite Envisions, LLC). VARTM was performed at room temperature, and the epoxy was set for 36 h to ensure proper curing. Composite strips with in-plane dimensions of 11 mm × 140 mm were prepared for tensile testing. Tabs were added to the sample per ASTM Standard D3039/D3039M. In order to contact the conductive fibers at the ends of the composite, silver paste was applied to exposed ends of the fabric, as described in the Supporting Information.

The composites were loaded in tension while measuring the electrical current in situ with a constant applied voltage of 5 V (Figure S6). The tensile stage used was an Instron 4301 with a  $\pm 10$  kN load cell (2525-804, Instron) and custom-made grips. The major principal strain  $(\varepsilon_1)$  in the sample was measured by 3D digital-image correlation (DIC),  $^{58-61}$  using Vic-3D 7 software (Correlated Solutions, Inc.) and two machine-vision cameras (GRAS 50S5M-C, Point Gray) with 75 mm lenses (HF75SA-1, Fujinon) and 10 mm extension tubes (Figure S7). A speckle pattern was painted on the sample for DIC (Figure S8) by air-brushing black paint speckles (carbon black color, Golden, Inc.) over a white paint background (titanium white color, Golden, Inc.).  $^{61}$ 

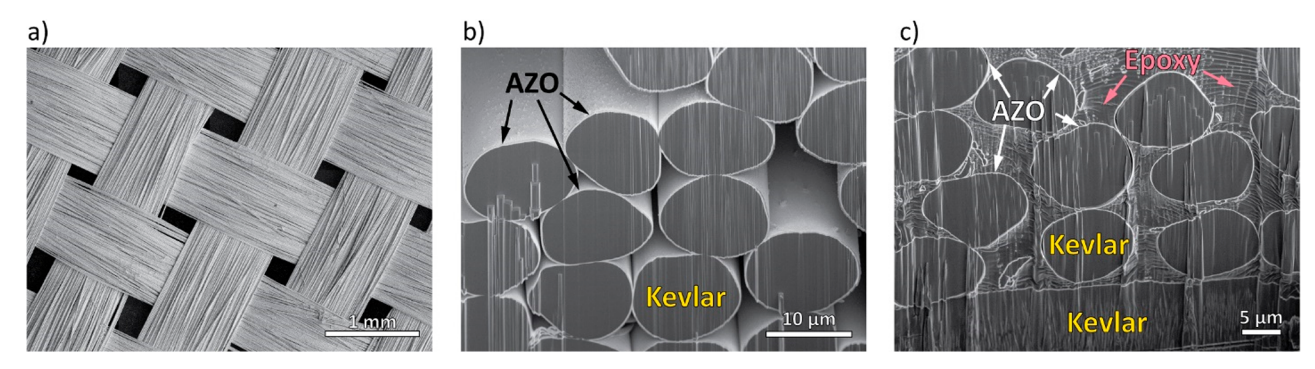


Figure 1. SEM image of (a) top-down view of K49 woven fabric coated with 200 nm of AZO, (b) SEM-PFIB cross section of K49 fabric coated with 200 nm of AZO, and (c) of 120 nm AZO-coated K49 fabrics embedded in epoxy after VARTM.

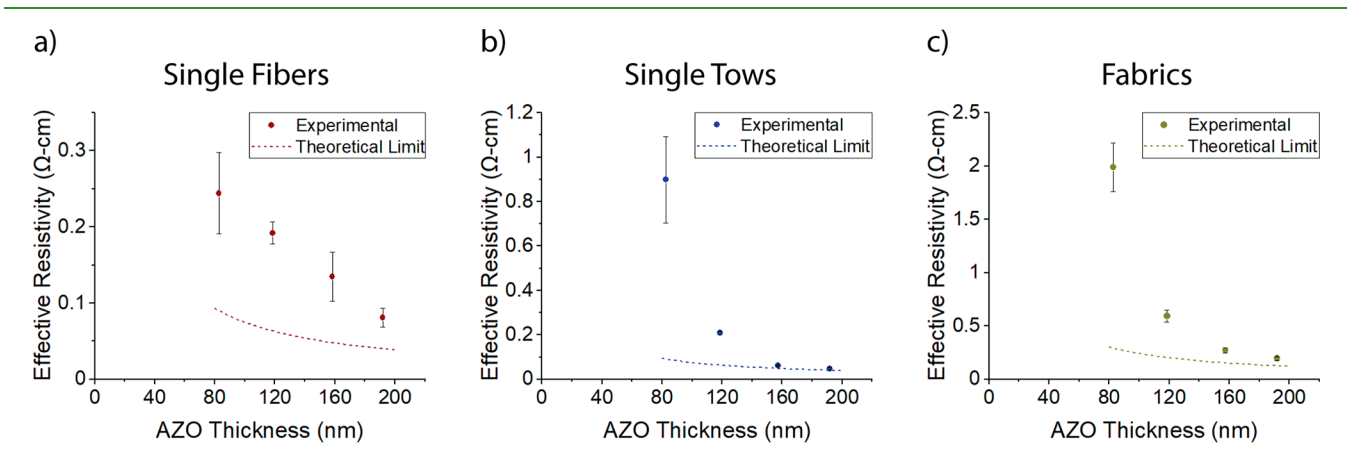


Figure 2. Experimental resistivity ( $\rho_e$ ) and theoretical limit of resistivity ( $\rho_t$ ) for (a) single fibers, (b) tows, and (c) fabrics coated with varying thicknesses of AZO.

## ■ RESULTS AND DISCUSSION

The targeted thicknesses of the AZO coatings on K49 were 80, 120, 160, and 200 nm. This was in close agreement with the measured thicknesses of 83, 119, 158, and 192 nm using spectroscopic ellipsometry on adjacent Si pieces. These measurements were also consistent with SEM-PFIB cross-sectional analysis of the coated fibers. The AZO coatings uniformly coated the entire surface of the exposed K49 fibers (Figure 1a,b). This illustrates the utility of ALD to enable conformal coatings with precise control of thickness on three-dimensional, high-surface-area fiber substrates with overlapping geometries. Furthermore, the coating is preserved after embedding the fibers in an epoxy matrix via VARTM (Figure 1c), demonstrating the applicability of this approach for interfacial engineering of PMCs.

The average resistivity of planar AZO films deposited on glass was measured to be 2.3 m $\Omega$ ·cm with a standard deviation of  $\pm 0.4$  m $\Omega$ ·cm using a four-point probe, <sup>57</sup> which is considered to be a material property of the coating. However, for the application of ALD coatings in multifunctional fabrics and composites, it is also meaningful to measure an effective resistivity, <sup>62–65</sup> based on the total cross-sectional area of the coated sample. The effective resistivity for single fibers, tows, and fabrics was calculated using eq 1:

$$\rho_{\rm e} = R \frac{A_{\rm eff}}{s} \tag{1}$$

where R is the experimentally measured resistance,  $A_{\text{eff}}$  the effective cross-sectional area, and s the probe spacing (s = 12

mm). The values of  $A_{\rm eff}$  for single fibers  $(A_{\rm fib})$ , tows  $(A_{\rm tow})$ , and woven fabrics  $(A_{\rm fab})$  are provided in the Supporting Information.

The measured values of effective resistivity can be compared to a theoretical limit, which would be the expected value if all of the coated surfaces in the 3-D geometry fully contribute to electrical conduction. The theoretical limit of effective resistivity is thus defined by eq 2:

$$\rho_{\rm t} = \rho_{\rm AZO} \frac{A_{\rm eff}}{A_{\rm AZO}} \tau_{\rm f} \tag{2}$$

where  $\rho_{\rm AZO}$  is the measured resistivity of planar AZO films, and  $A_{\rm AZO}$  is the cross-sectional area of only the AZO coating;  $\tau_{\rm f}$  is a tortuosity factor that takes into account the fact that in a woven fabric, the total length of the individual fibers is longer than the fabric length because of the waviness of the weave. The  $\tau_{\rm f}$  for the fibers and the tows was 1, and the  $\tau_{\rm f}$  of the woven fabric was estimated to be 1.006 based on the weave geometry.

The measured  $\rho_{\rm e}$  values for the fibers, tows, and fabrics as a function of AZO thickness are shown in Figure 2. For all three sample geometries, the average  $\rho_{\rm e}$  monotonically decreases as the thickness of the coating increases. This is expected, because  $A_{\rm AZO}$  increases as the ALD coating thickness increases.

As observed in Figure 2a, deviations between  $\rho_{\rm e}$  and  $\rho_{\rm t}$  for the single fibers are observed. We hypothesize that this deviation is a result of microscopic cracks or flaws present in the coating along the fiber length, which likely form during the sensitive handling of single fibers. The theoretical limit assumes the ALD coating to be a perfectly continuous shell.

Figure 3. (a) SEM-PFIB imaging of three parallel K49 fiber coated with 200 nm of AZO with bridged connections and (b) a top-down view of a K49 fiber coated with 120 nm of ZnO after merged parallel fibers detached (orange false color added to highlight exposed surface of K49 fibers). Schematic of K49 fibers with bridged AZO coatings (c) 80 nm and (d) 200 nm thick that are equally spaced.

Therefore, any microscopic flaw, such as a crack, will result in a "bottleneck" for local current flow (Figure S9), increasing the measured resistance. When the thickness of the coating was further reduced to 40 nm, an order-of-magnitude increase in  $\rho_{\rm e}$  was observed (Table S1). Therefore, 80 nm was chosen as the minimal thickness to achieve sufficiently low electrical resistivity in this study.

The tows exhibit a similar trend of decreasing  $\rho_{\rm e}$  with increasing ALD film thickness. As the thickness increases,  $\rho_{\rm e}$  converges to  $\rho_{\rm t}$  (Figure 2b). However, for thinner coatings, the deviation between  $\rho_{\rm e}$  and  $\rho_{\rm t}$  increases substantially. For example, the tows coated with 158 and 192 nm of AZO exhibit a percent difference of 24.3% and 15.7%, respectively (further details are in the Supporting Information). Comparatively, the percent difference for the tows coated with 83 nm of AZO was almost 900%.

The dependence of  $\rho_e$  on thickness for the tows can be rationalized by considering the interconnectivity of adjacent fibers in the tow. This interconnected network between adjacent fibers in a tow allows for additional charge pathways and improved percolation, which reduces the resistivity of the sample. In the limit that all fibers within the tow fully contribute to the conductance,  $\rho_e$  converges to  $\rho_r$ .

The interconnectivity between fibers can be visualized using SEM-PFIB imaging (Figure 3a,b). Figure 3a shows a cross section of multiple adjacent fibers within a tow, where the ALD shell merges and forms contact points. Figure 3b shows a region of a shell in a fiber that had detached from an adjacent fiber during handling. Grooves along the longitudinal direction are associated with prior line contacts between two cylindrical fibers, and a local delamination is visible along one of the grooves, indicating that the continuous ALD shell detached when the adjacent fiber was removed.

Thicker AZO coatings will facilitate a higher number of bridged connections, enhancing percolation and improving the conductive properties of the coated tows. Furthermore, thicker coatings are more likely to have a larger bridged contact area for each connection point (Figure 3c,d), which would reduce the contact resistance between adjacent fibers. These bridged connections between fibers will also make the conductive pathway more "defect tolerant", because if a bottleneck to current flow (such as a flaw in the ALD coating) exists along a single fiber, the current can follow a parallel pathway. This can help to rationalize the observation of improved agreement between  $\rho_{\rm e}$  and  $\rho_{\rm t}$  for thicker coatings (160–200 nm) in the tows (Figure 2b) compared to the single fibers (Figure 2a). A quantitative comparison of the percent difference for single fibers, tows, and fabrics with varying thicknesses is provided in Table S2.

In addition to the fiber-fiber contact resistance, another factor that will influence the experimentally measured  $\rho_e$  is the contact to the metal electrodes used for the electrical resistance measurements. To form a metal contact in this study, silver paint was applied to the fibers, tows, and fabrics. While the liquid paint can diffuse into larger voids between fibers, interior fibers in the tows and fabrics will rely on fiber-to-fiber bridged connections in order to contribute to the overall conductive network (Figure S10). Thicker coatings increase the probability and number of sites with bridged connections, which increases the interconnectivity within the tows and fabrics. The fact that the metal contact does not directly contact each individual fiber amplifies the deviation between  $\rho_{\rm e}$ and  $\rho_{\rm t}$  with decreasing thickness, because only those fibers within the network that have a pathway to the electrode will contribute to conduction. This further highlights the importance of the electrical contact in manufacturing multifunctional composites where the functional layer is confined to the interphase region.

Trends similar to those observed for the individual tows were observed in the resistivity data for the woven fabrics (Figure 2c). As the coating thickness increases, the measured  $\rho_{\rm e}$  values converge to the theoretical limit. For example, the difference between  $\rho_{\rm e}$  and  $\rho_{\rm t}$  for the fabrics coated with 158 and 192 nm films was 64.8% and 44.7%, respectively. Once again, owing to the percolation effects described above, these values are closer to the theoretical limit than the corresponding values for single fibers. However, in addition to the improved percolation within a tow, for the woven fabric, there are also tow-to-tow contact regions that overlap between the longitudinal and transverse weave directions.

Overlapping, perpendicular fibers that contact one another also contain bridged AZO connections, as confirmed by SEM imaging (Figure S11). Because of this overlapping geometry, the electrical current may follow multiple paths. For simplicity, one of the assumptions made for the theoretical limit  $(\rho_t)$  of the fabrics was that only longitudinally aligned tows (0° direction) contribute to the resistance, whereas the transversely aligned tows (90° direction) did not. This is a reasonable assumption because the contacts were formed such that the applied voltage was along the longitudinal direction, which explains the good convergence between the experimental and theoretical values in this study. However, as the complexity of the fabric network increases (such as nonorthotropic weaves), electrical transport within the fabrics will be determined by a weighted statistical distribution over all possible charge paths.

In addition to the fabrics, the conductive properties of PMCs were analyzed after embedding the coated fabrics in an

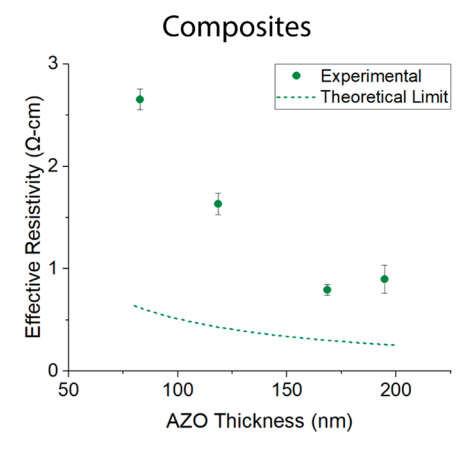


**Figure 4.**  $\rho_{\rm e}$  and  $\rho_{\rm t}$  values for fabricated composites using fabrics coated with different thicknesses of AZO (calculated using eq 1 and 2, where s=114 mm).

epoxy matrix via the VARTM process. The  $\rho_{\rm e}$  of the composites follows the same trend that was observed with the woven fabrics up to 160 nm, indicating that the electrical properties were preserved after fabrication (Figure 4). The 200 nm thick sample exhibited a slight increase in the average and standard deviation of effective resistivity, which we attribute to minor damage of the coating as a result of slight bending during the handling process after fabrication. The single-ply composite (which is approximately 0.2 mm thick) is prone to bending during manufacturing. Thicker coatings have a lower critical stress for onset of cracking and are more likely to fracture as a consequence of this bending strain, which can explain the slightly higher variation in  $\rho_{\rm e}$  observed for the thickest coating. The relationships between thickness of the coating and its fracture behavior will be discussed in further detail later.

We note that the VARTM process applies a compressive pressure to the composite during vacuum infiltration of the epoxy into the fabric. This could potentially cause damage to the coating if the critical stress for onset of cracking of the coating is exceeded. Furthermore, applied compression has previously been shown to enhance the overall conductivity of ALD-coated fabrics as a result of enhanced fiber—fiber contact. However, the resin could potentially flow between adjacent fibers during infiltration, reducing the total fiber—fiber

contact points. To counteract these effects, bridged connections likely play an important role in maintaining the conductive properties of the composite. In summary, there are multiple competing factors that can dictate the conductance of PMCs that use coated woven fabrics. Overall, the electrical conductivity imparted by the coatings was largely preserved after the VARTM process, which is consistent with cross-sectional SEM analysis (Figure 1c).

To study the mechanical response of the ALD-modified composites, the samples were mechanically loaded in tension until failure. This allowed for a determination of the impact that the coatings had on the bulk stress-strain response (Figure 5). The samples all fractured within the gauge region. In the uncoated sample, a slight nonlinearity was observed in the stress-strain response, where the modulus increases with increasing strain up to ~2.0%, after which linear-elastic behavior is observed. This "tension-stiffening" effect may be attributed to straightening of the woven fibers in the longitudinal direction under applied tension. In contrast, the coated composites exhibit a linear-elastic response above ~0.4% strain. We hypothesize that the AZO coatings may contribute to this improved linearity at lower strains as a result of the bridged connections, which provide a "pinning" effect that could increase the shear resistance and restrict the sliding of the fibers. In general, the modulus of the coated samples had minimal variation with respect to the control sample. Furthermore, the experimental stress-strain response from these experiments was within a consistent range of expected modulus values based on the fiber volume fraction (0.25-0.30) and modulus of K49 (112 GPa, DuPont de Nemours, Inc.) and epoxy (1.26 GPa, Composite Envisions, LLC).

No clear correlation between the AZO thickness and the ultimate tensile strength or ultimate tensile strain were observed. In general, the modulus of the coated samples had minimal variations of  $\pm 14\%$  with respect to the control sample. The modulus varied between 12 and 16 GPa from the control sample, which was 14 GPa. There was no discernible trend with increasing thickness. Additional tensile test results for the bare and 120 nm coated samples can be found in Figure S12. These results demonstrate that ALD is an effective means of imparting multifunctionality into PMCs, which can be achieved without deleterious effects on their bulk mechanical properties.

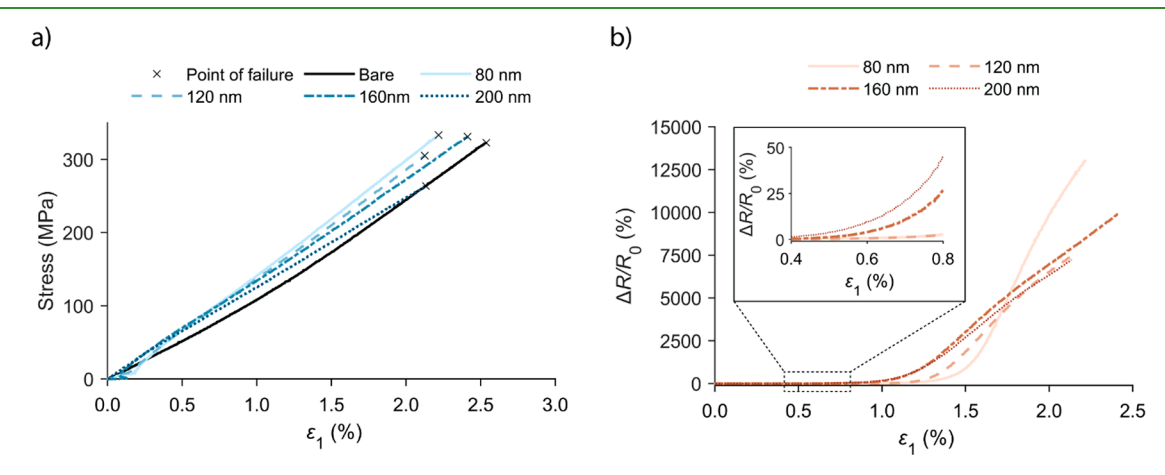
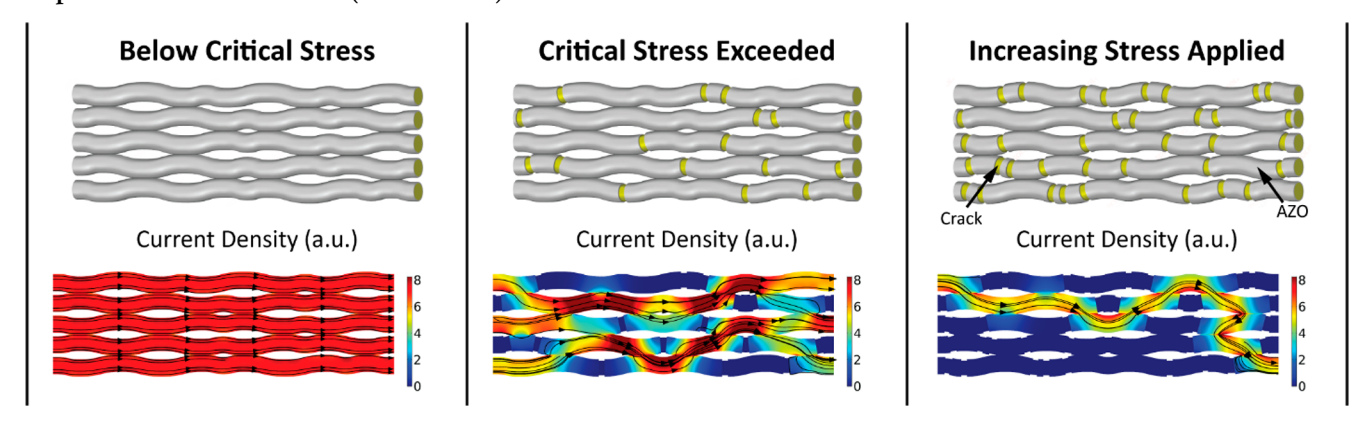


Figure 5. (a) Stress-strain curves and (b)  $\Delta R/R_0$  -strain curves for K49-epoxy composites with varying thicknesses of AZO coatings on the K49 fabrics

Figure 6. Post-mortem SEM cross section of a composite loaded to failure, with K49 fabric coated with 120 nm of AZO. The load was applied horizontally with respect to the plane of the image. (Selective adjustments of contrast and brightness were done to highlight the cracks).

Scheme 1. Schematic Illustration and Associated COMSOL Model for Qualitative Visualization of Charge Pathways within a Simplified Tow of Five Fibers (Not to Scale)<sup>a</sup>



"(Left) Representative behavior of a coated fabric with no applied load. (Middle) As the load increases and cracks begin to form in the coating, the path of least resistance will be facilitated by alternative pathways through bridged connections between fibers, resulting in an increase in resistance. (Right) Upon further loading, an increased density of cracks will result in fewer viable conductive paths, increasing the tortuosity of viable charge pathways and the associated resistance.

The *in situ* electrical response of the PMCs as a function of applied strain was also studied. A significant change in the measured electrical resistance was observed under increased tensile loading (Figure 5b). This change was quantified according to eq 3:

$$\frac{\Delta R}{R_0} = \frac{R(\varepsilon_1) - R_0}{R_0} \tag{3}$$

where  $R(\varepsilon_1)$  is the measured resistance as a function of strain, and  $R_0$  is the initial resistance at a strain value of zero.

 $\Delta R/R_0$  was observed to increase as the principal strain ( $\varepsilon_1$ ) increased (Figure 5b). To investigate the origins of this increase in resistance, post-mortem SEM-PFIB imaging was performed. Figure 6 shows a cross section of an exposed ALD coating on a fiber surface, where the tensile load was applied in the horizontal direction (along the fiber axis). Channel cracks in the coating are observed, which primarily occur along the circumference of the fiber (perpendicular to the applied load). We attribute the increased resistance under tension to the formation of these cracks, which impede current flow and decrease the number of continuous charge pathways. However, the composite can maintain some of its conductivity even after cracks have formed, because the bridged connections between the fibers enable alternative pathways for current flow throughout the interconnected network.

The impact of crack formation in the coating on electrical transport within the composite is illustrated in Scheme 1. According to the principles of thin-film fracture mechanics, when the critical stress for the onset of fracture is reached within the coating, crack formation will initiate. As strain

continues to increase, additional cracks will form, which further disrupts the electrical conduction pathways.<sup>68</sup>

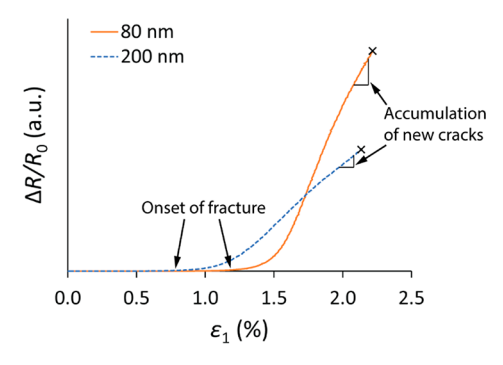
To provide a qualitative visual-aid of these trends, a 3-D model was developed using COMSOL Multiphysics (Scheme 1). The model is simplified, using only five fibers aligned along a plane. The applied voltage at the boundaries was consistent among the three panels. In the left panel of Scheme 1, before the onset of cracking, the current flows uninterrupted along the continuous coating. As cracks begin to form, the electrical resistance of the individual fibers increases. In the extreme case where a circumferential crack completely isolates two sections of the coating, the current flow through an individual fiber will halt. As a consequence of these increases in the resistance of individual fibers, the path of least resistance through the fiber network will evolve. Specifically, bridged connections between adjacent fibers are required to provide alternative pathways.

As the number of cracks grows under increasing stress, the number of possible pathways will continue to decrease, resulting in a monotonic increase in the electrical resistance. The tows in the K49 fabric used in this study contain over 200 fibers that are closely packed, which allows for the composite to maintain a percolated network of charge pathways even when the crack density along the AZO coating is significant. This is analogous to the increased tolerance to defects for tows and fabrics described previously, where bridged connections between fibers can compensate for bottlenecks to current flow within single fibers.

As described above, the electrical response as a function of strain in the composites varied with the thickness of the coating (Figure 5b). Initially, there is minimal change in resistance with strain. As the strain increases to approximately 0.4%–1.0%, a gradual increase in  $\Delta R/R_0$  is observed, with an

earlier onset for samples with thicker coatings. As the strain continues to rise, we observe a further increase in the slope of  $\Delta R/R_0$ . The slope of the curve in this higher-strain range (greater than 1.5%) becomes larger as the film thickness decreases. At the point where bulk fracture of the composite occurs, the final value of  $\Delta R/R_0$  monotonically decreases with increasing coating thickness. These observations, which are summarized in Scheme 2, suggest that multiple competing factors are at play when determining the thickness dependence of  $\Delta R/R_0$ .

Scheme 2. Representative  $\Delta R/R_0$  vs Strain Curves for PMCs with Thin (80 nm) and Thick (200 nm) AZO Coatings<sup>a</sup>



<sup>a</sup>The onset fracture of the coating occurs sooner for the thicker coating. As strain continues to increase, both the accumulation of cracks and the rate increase of the electrical resistance will be larger for the thin coating.

To rationalize the competing effects in the cracking behavior for different coating thicknesses, we consider the theory of fracture mechanics of thin films on infinitely large substrates. A channeling crack will propagate in the coating at a critical onset stress. The coated fabric is modeled as a homogeneous linearelastic system, because the Young's modulus of K49 fibers (112 GPa) is sufficiently close to the Young's modulus of ZnO (143 GPa).<sup>69</sup> The embedded epoxy has a lower modulus of 1.26 GPa, and thus, for simplicity it was not considered in this analysis. The critical stress in the coating  $(\sigma_c)$  can then be described as follows:66,67

$$\sigma_{\rm c} = \sqrt{\frac{K_{\rm lc}^2}{1.98t}} \tag{4}$$

where  $K_{Ic}$  is the mode-I fracture toughness under plane-strain conditions and t is the thickness of the coating. Because  $\sigma_{\rm c} \propto 1/t^{0.5}$ , thicker coatings will have a lower critical stress. This correlates well with our experimental observations, wherein the initial increase in  $\Delta R/R_0$  occurs at lower strain values as the coating thickness increases (Figure 5b and Scheme 2). We note that this initial increase will be statistical in nature, because the local stress along the individual fibers (as well as the initial defect distribution within the coatings) will vary slightly throughout the woven composite. However, the cumulative effect of multiple fibers experiencing the onset of fracture at low strain values will result in the net increase in measured resistance.

As the strain in the samples continuously increases, a sharper rise of the slope of  $\Delta R/R_0$  vs strain is observed as the coating thickness decreases (Figure 5b and Scheme 2). The formation of additional cracks in the film depends on the stress and the intercrack spacing. Both of these factors depend on the coating

thickness. Previous modeling work has described the theoretical equilibrium crack spacing  $(s_{\text{equil}})$  for a linear-elastic, homogeneous system with a perfectly bonded interface.<sup>68</sup> This can be expressed as

$$\frac{s_{\text{equil}}}{t} = 5.6 \sqrt{\frac{K_{\text{lc}}}{\sigma_{\text{f}}^2 t}} \tag{5}$$

where  $\sigma_{\rm f}$  is the stress in the coating. Contrary to eq 4,  $s_{\rm equil} \propto t^{0.5}$ . Therefore,  $s_{\rm equil}$  will be larger for thicker films. This is consistent with the observation that the measured resistance of the composites rises faster with applied strain in the composite samples with thinner films. As shown in Scheme 1, as intercrack spacing decreases, the pathway for electronic transport becomes more limited. An additional contributing factor to this trend is the fact that composites with thicker coatings have a higher number of bridged connections, forming a more robust percolation network. This also helps to explain the fact that the final measured  $\Delta R/R_0$  after bulk fracture of the composite is lower for thicker coatings.

The relationships described herein between strain and electrical conduction can be used in the future to guide and inform the design of PMCs with interfacial coatings using ALD. In particular, we identify the acceptable strain limits under an applied load that are allowable to maintain sufficient conductivity (and continuity), which can be adjusted by varying the coating thickness. Depending on the targeted application, this may also lead to design trade-offs, where control of thickness may also be important to the functionality itself. For example, as we show in Figures 2 and 4, effective resistivity decreases with increasing thickness. In applications where a large electrical current is passed, a lower resistance may be needed to avoid a large voltage drop and excessive Joule heating, which may necessitate a thicker coating. As shown in Figure 5b, while thicker coatings maintain a higher fraction of their initial conductivity at failure, they start to deviate in resistivity at lower strains. Therefore, depending on the predicted load profile that the composite will experience during service, this sets up a multidimensional optimization problem.

In addition to the coating serving as a component in a multifunctional composite, the change in resistance with strain could also be used for structural health monitoring. Because cracking leads to permanent changes in  $\Delta R/R_0$ , the resistance can serve as a record of maximum load experienced during operation. The sensitivity of this increase can be tuned by varying the coating thickness. This could be particularly useful as a signal to warn of the potential for catastrophic failure, because the range of  $\Delta R/R_0$  spans several orders of magnitude before bulk fracture of the composite occurs. Because the coating has minimal impact on the elastic response of the coating (Figure 5a), this change in resistance can provide a warning signal as we approach catastrophic failure (Figure 5b).

#### CONCLUSION

This work demonstrated the ability to impart electrical conductivity into electrically insulating fibers, fabrics, and PMCs through interfacial modification by ALD. The use of ALD facilitates subnanometer precision in coating thickness on complex fabrics, which can be used to tune the effective resistivity. Specifically, we show that the influence of thickness on resistivity depends on both the conduction through individual fibers, as well as the percolation through a fiber

network, which is dependent on the number of bridged connections. This percolation effect allows for increased tolerance to defects in individual fibers, as bridged connections provide alternative current pathways that do not exist at the single-fiber level.

The conductive properties of the coated fabrics were maintained after they were embedded in an epoxy matrix using the VARTM method, illustrating the utility of this approach for the design and manufacturing of multifunctional composites. The composites were loaded in tension to failure, and the resulting changes in the electrical resistance were observed. These changes were attributed to crack formation in the conductive coating. The relative change in resistance was studied as a function of thickness, and two competing effects were observed. Specifically, the onset of cracking at low strain values occurs earlier as the coating thickness increases. However, the rate of increase in crack formation at larger strains was faster as thickness decreases. Additionally, the samples with the thicker coatings have a larger number of bridged connections, which helps to maintain electrical conductance even as cracks form. Knowledge of these coupled relationships between thickness, strain, and fracture is important to the design and implementation of ALD-modified PMCs as multifunctional structural materials.

Overall, the insights from this study can be useful when designing multifunctional composites. Specifically, the influence of coating thickness on the coupled electrical and mechanical response of the system can define the limits of useful operation, which may also be useful for structural health monitoring. In this study, AZO was selected as a model system owing to its high electrical conductivity. However, given the diverse set of materials that can be deposited by ALD, this platform can be extended in the future to manufacture more complex devices within a composite framework, including electronics, energy storage, and optoelectronics. Beyond tuning the functional properties of the coating materials, this work also illustrates the importance of thin-film mechanics in designing such devices, which must be simultaneously optimized to ensure optimal performance under the targeted loading conditions.

## ASSOCIATED CONTENT

#### Supporting Information

The Supporting Information is available free of charge at https://pubs.acs.org/doi/10.1021/acsapm.1c01236.

Additional experimental details, calculation of crosssectional area, XPS and XRD analysis, electrical measurement details, VARTM setup, DIC setup and details, additional SEM analysis, and table of differences between theoretical and measured effective resistivities (PDF)

#### AUTHOR INFORMATION

#### **Corresponding Author**

Neil P. Dasgupta — Department of Mechanical Engineering and Department of Materials Science and Engineering, University of Michigan, Ann Arbor, Michigan 48109, United States; orcid.org/0000-0002-5180-4063;

Email: ndasgupt@umich.edu

#### **Authors**

- Robin E. Rodríguez Department of Mechanical Engineering, University of Michigan, Ann Arbor, Michigan 48109, United States
- Tae Hwa Lee Department of Mechanical Engineering, University of Michigan, Ann Arbor, Michigan 48109, United States
- Yuxin Chen Department of Mechanical Engineering, University of Michigan, Ann Arbor, Michigan 48109, United States
- Eric Kazyak Department of Mechanical Engineering, University of Michigan, Ann Arbor, Michigan 48109, United States; © orcid.org/0000-0001-5099-3985
- Claire Huang Department of Mechanical Engineering, University of Michigan, Ann Arbor, Michigan 48109, United States
- Tae H. Cho Department of Mechanical Engineering, University of Michigan, Ann Arbor, Michigan 48109, United States
- William S. LePage Department of Mechanical Engineering, University of Michigan, Ann Arbor, Michigan 48109, United States; Present Address: Department of Mechanical Engineering, The University of Tulsa, Tulsa, OK 74104
- M. D. Thouless Department of Mechanical Engineering and Department of Materials Science and Engineering, University of Michigan, Ann Arbor, Michigan 48109, United States
- Mihaela Banu Department of Mechanical Engineering, University of Michigan, Ann Arbor, Michigan 48109, United States

Complete contact information is available at: https://pubs.acs.org/10.1021/acsapm.1c01236

#### Notes

The authors declare no competing financial interest.

### ACKNOWLEDGMENTS

This work was supported by the Air Force Office of Scientific Research (AFOSR) under Grant FA9550-16-1-0313. This material is based upon work supported by the National Science Foundation under Grant No. 1751590. The authors acknowledge the financial support of the University of Michigan College of Engineering and NSF Grant #DMR-9871177 and technical support from the Michigan Center for Materials Characterization and the Lurie Nanofabrication Facility. The authors also thank Andrea Poli for assistance with the mechanical measurements, Julia Lenef for help with the materials characterization, and Brendan Patterson and Prof. Henry Sodano for advice on fiber preparation.

## ABBREVIATIONS

ALD, atomic layer deposition; CVD, chemical vapor deposition; DEZ, diethyl zinc; DIC, digital image correlation; DMAI, dimethylaluminum isopropoxide; EPD, electrophoretic deposition; FRC, fiber-reinforced composite; PFIB, plasma focused-ion beam; PMC, polymer-matrix composite; SEM, scanning electron microscopy; VARTM, vacuum-assisted resin-transfer-molding; XPS, X-ray photoelectron spectroscopy; XRD, X-ray diffraction

## REFERENCES

(1) González, C.; Vilatela, J. J.; Molina-Aldareguía, J. M.; Lopes, C. S.; LLorca, J. Structural Composites for Multifunctional Applications:

- Current Challenges and Future Trends. Prog. Mater. Sci. 2017, 89, 194-251.
- (2) Xiao, Y.; Qiao, W.; Fukuda, H.; Hatta, H. The Effect of Embedded Devices on Structural Integrity of Composite Laminates. *Compos. Struct.* **2016**, *153*, 21–29.
- (3) Deka, B. K.; Hazarika, A.; Kim, J.; Park, Y.-B.; Park, H. W. Multifunctional CuO Nanowire Embodied Structural Supercapacitor Based on Woven Carbon Fiber/Ionic Liquid—Polyester Resin. *Composites, Part A* **2016**, *87*, 256–262.
- (4) Asp, L. E.; Greenhalgh, E. S. Structural Power Composites. Compos. Sci. Technol. 2014, 101, 41-61.
- (5) Wen, J.; Xia, Z.; Choy, F. Damage Detection of Carbon Fiber Reinforced Polymer Composites via Electrical Resistance Measurement. *Composites, Part B* **2011**, 42 (1), 77–86.
- (6) Alexopoulos, N. D.; Bartholome, C.; Poulin, P.; Marioli-Riga, Z. Structural Health Monitoring of Glass Fiber Reinforced Composites Using Embedded Carbon Nanotube (CNT) Fibers. *Compos. Sci. Technol.* **2010**, *70* (2), 260–271.
- (7) Chung, D. D. L.; Wang, S. Carbon Fiber Polymer-Matrix Structural Composite as a Semiconductor and Concept of Optoelectronic and Electronic Devices Made from It. *Smart Mater. Struct.* **1999**, 8 (1), 161–166.
- (8) Wu, J.; Chen, J.; Zhao, Y.; Liu, W.; Zhang, W. Effect of Electrophoretic Condition on the Electromagnetic Interference Shielding Performance of Reduced Graphene Oxide-Carbon Fiber/Epoxy Resin Composites. *Composites, Part B* **2016**, *105*, 167–175.
- (9) Chen, J.; Wu, J.; Ge, H.; Zhao, D.; Liu, C.; Hong, X. Reduced Graphene Oxide Deposited Carbon Fiber Reinforced Polymer Composites for Electromagnetic Interference Shielding. *Composites, Part A* **2016**, *82*, 141–150.
- (10) Brown, E.; White, S.; Sottos, N. Retardation and Repair of Fatigue Cracks in a Microcapsule Toughened Epoxy Composite—Part II: In Situ Self-Healing. *Compos. Sci. Technol.* **2005**, *65* (15–16), 2474–2480.
- (11) Yin, T.; Rong, M. Z.; Zhang, M. Q.; Yang, G. C. Self-Healing Epoxy Composites Preparation and Effect of the Healant Consisting of Microencapsulated Epoxy and Latent Curing Agent. *Compos. Sci. Technol.* **2007**, *67* (2), 201–212.
- (12) Kessler, M. R.; Sottos, N. R.; White, S. R. Self-Healing Structural Composite Materials. *Composites, Part A* **2003**, 34 (8), 743–753.
- (13) Vilatela, J. J.; Eder, D. Nanocarbon Composites and Hybrids in Sustainability: A Review. *ChemSusChem* **2012**, *5* (3), 456–478.
- (14) Zhang, D.; Ye, L.; Deng, S.; Zhang, J.; Tang, Y.; Chen, Y. CF/EP Composite Laminates with Carbon Black and Copper Chloride for Improved Electrical Conductivity and Interlaminar Fracture Toughness. *Compos. Sci. Technol.* **2012**, 72 (3), 412–420.
- (15) Gungor, S.; Bakis, C. E. Indentation Damage Detection in Glass/Epoxy Composite Laminates with Electrically Tailored Conductive Nanofiller. *J. Intell. Mater. Syst. Struct.* **2016**, 27 (5), 679–688.
- (16) Müller, M.; Pötzsch, H.; Gohs, U.; Heinrich, G. Online Structural-Health Monitoring of Glass Fiber-Reinforced Thermoplastics Using Different Carbon Allotropes in the Interphase. *Materials* **2018**, *11* (7), 1075.
- (17) Nasser, J.; Groo, L.; Zhang, L.; Sodano, H. Laser Induced Graphene Fibers for Multifunctional Aramid Fiber Reinforced Composite. *Carbon* **2020**, *158*, 146–156.
- (18) Groo, L.; Nasser, J.; Inman, D.; Sodano, H. Laser Induced Graphene for in Situ Damage Sensing in Aramid Fiber Reinforced Composites. *Compos. Sci. Technol.* **2021**, 201, 108541.
- (19) Coleman, J. N.; Curran, S.; Dalton, A. B.; Davey, A. P.; McCarthy, B.; Blau, W.; Barklie, R. C. Percolation-Dominated Conductivity in a Conjugated-Polymer-Carbon-Nanotube Composite. *Phys. Rev. B: Condens. Matter Mater. Phys.* **1998**, 58 (12), R7492—R7495.
- (20) Díez-Pascual, A. M.; Naffakh, M.; Marco, C.; Gómez-Fatou, M. A.; Ellis, G. J. Multiscale Fiber-Reinforced Thermoplastic Composites

- Incorporating Carbon Nanotubes: A Review. Curr. Opin. Solid State Mater. Sci. 2014, 18 (2), 62–80.
- (21) Lee, S.; Ko, K.; Youk, J.; Lim, D.; Jeong, W. Preparation and Properties of Carbon Fiber/Carbon Nanotube Wet-Laid Composites. *Polymers (Basel, Switz.)* **2019**, *11* (10), 1597.
- (22) Ehlert, G. J.; Sodano, H. A. Fiber Strain Sensors from Carbon Nanotubes Self-Assembled on Aramid Fibers. *J. Intell. Mater. Syst. Struct.* **2014**, 25 (17), 2117–2121.
- (23) Sandler, J.; Shaffer, M. S. P.; Prasse, T.; Bauhofer, W.; Schulte, K.; Windle, A. H. Development of a Dispersion Process for Carbon Nanotubes in an Epoxy Matrix and the Resulting Electrical Properties. *Polymer* **1999**, *40* (21), 5967–5971.
- (24) Bauhofer, W.; Kovacs, J. Z. A Review and Analysis of Electrical Percolation in Carbon Nanotube Polymer Composites. *Compos. Sci. Technol.* **2009**, *69* (10), 1486–1498.
- (25) Puch, F.; Hopmann, C. Morphology and Tensile Properties of Unreinforced and Short Carbon Fibre Reinforced Nylon 6/Multiwalled Carbon Nanotube-Composites. *Polymer* **2014**, *55* (13), 3015–3025
- (26) Nguyen-Tran, H. D.; Hoang, V. T.; Do, V. T.; Chun, D. M.; Yum, Y. J. Effect of Multiwalled Carbon Nanotubes on the Mechanical Properties of Carbon Fiber-Reinforced Polyamide-6/Polypropylene Composites for Lightweight Automotive Parts. *Materials* **2018**, *11* (3), 429.
- (27) Bai, J. B.; Allaoui, A. Effect of the Length and the Aggregate Size of MWNTs on the Improvement Efficiency of the Mechanical and Electrical Properties of Nanocomposites—Experimental Investigation. *Composites, Part A* **2003**, 34 (8), 689–694.
- (28) Sharma, S. P.; Lakkad, S. C. Effect of CNTs Growth on Carbon Fibers on the Tensile Strength of CNTs Grown Carbon Fiber-Reinforced Polymer Matrix Composites. *Composites, Part A* **2011**, 42 (1), 8–15.
- (29) Sager, R. J.; Klein, P. J.; Lagoudas, D. C.; Zhang, Q.; Liu, J.; Dai, L.; Baur, J. W. Effect of Carbon Nanotubes on the Interfacial Shear Strength of T650 Carbon Fiber in an Epoxy Matrix. *Compos. Sci. Technol.* **2009**, *69* (7–8), 898–904.
- (30) Garcia, E.; Wardle, B.; Johnhart, A.; Yamamoto, N. Fabrication and Multifunctional Properties of a Hybrid Laminate with Aligned Carbon Nanotubes Grown In Situ. *Compos. Sci. Technol.* **2008**, *68* (9), 2034–2041
- (31) Park, J. K.; Do, I. H.; Askeland, P.; Drzal, L. T. Electro-deposition of Exfoliated Graphite Nanoplatelets onto Carbon Fibers and Properties of Their Epoxy Composites. *Compos. Sci. Technol.* **2008**, *68* (7–8), 1734–1741.
- (32) Jur, J. S.; Spagnola, J. C.; Lee, K.; Gong, B.; Peng, Q.; Parsons, G. N. Temperature-Dependent Subsurface Growth during Atomic Layer Deposition on Polypropylene and Cellulose Fibers. *Langmuir* **2010**, *26* (11), 8239–8244.
- (33) Hyde, G. K.; Scarel, G.; Spagnola, J. C.; Peng, Q.; Lee, K.; Gong, B.; Roberts, K. G.; Roth, K. M.; Hanson, C. A.; Devine, C. K.; Stewart, S. M.; Hojo, D.; Na, J.-S.; Jur, J. S.; Parsons, G. N. Atomic Layer Deposition and Abrupt Wetting Transitions on Nonwoven Polypropylene and Woven Cotton Fabrics. *Langmuir* **2010**, *26* (4), 2550–2558.
- (34) Gregorczyk, K. E.; Pickup, D. F.; Sanz, M. G.; Irakulis, I. A.; Rogero, C.; Knez, M. Tuning the Tensile Strength of Cellulose through Vapor-Phase Metalation. *Chem. Mater.* **2015**, 27 (1), 181–188.
- (35) Daubert, J. S.; Mundy, J. Z.; Parsons, G. N. Kevlar-Based Supercapacitor Fibers with Conformal Pseudocapacitive Metal Oxide and Metal Formed by ALD. *Adv. Mater. Interfaces* **2016**, 3 (21), 1600355.
- (36) Militzer, C.; Dill, P.; Goedel, W. A. Atomic Layer Deposition onto Carbon Fiber Fabrics. *J. Am. Ceram. Soc.* **2017**, *100* (12), 5409–5420.
- (37) Dasgupta, N. P.; Lee, H.-B.-R.; Bent, S. F.; Weiss, P. S. Recent Advances in Atomic Layer Deposition. *Chem. Mater.* **2016**, 28 (7), 1943–1947.

- (38) Miikkulainen, V.; Leskelä, M.; Ritala, M.; Puurunen, R. L. Crystallinity of Inorganic Films Grown by Atomic Layer Deposition: Overview and General Trends. *J. Appl. Phys.* **2013**, *113* (2), No. 021301.
- (39) Zeng, L.; Liu, X.; Chen, X.; Soutis, C. Surface Modification of Aramid Fibres with Graphene Oxide for Interface Improvement in Composites. *Appl. Compos. Mater.* **2018**, 25 (4), 843–852.
- (40) Rodríguez, R. E.; Cho, T. H.; Ravandi, M.; LePage, W. S.; Banu, M.; Thouless, M. D.; Dasgupta, N. P. Mechanical Properties of Fibers Coated by Atomic Layer Deposition for Polymer-Matrix Composites with Enhanced Thermal and Ultraviolet Resistance. In *Minerals, Metals and Materials Series*; Springer, 2020; pp 1513–1527. DOI: 10.1007/978-3-030-36296-6 140.
- (41) Xiao, X.; Cao, G.; Chen, F.; Tang, Y.; Liu, X.; Xu, W. Durable Superhydrophobic Wool Fabrics Coating with Nanoscale Al2O3 Layer by Atomic Layer Deposition. *Appl. Surf. Sci.* **2015**, 349, 876–879.
- (42) Kim, G.-M.; Lee, S.-M.; Michler, G. H.; Roggendorf, H.; Gösele, U.; Knez, M. Nanostructured Pure Anatase Titania Tubes Replicated from Electrospun Polymer Fiber Templates by Atomic Layer Deposition. *Chem. Mater.* **2008**, *20* (9), 3085–3091.
- (43) Lee, S.-M.; Pippel, E.; Gosele, U.; Dresbach, C.; Qin, Y.; Chandran, C. V.; Brauniger, T.; Hause, G.; Knez, M. Greatly Increased Toughness of Infiltrated Spider Silk. *Science (Washington, DC, U. S.)* 2009, 324 (5926), 488–492.
- (44) Azpitarte, I.; Zuzuarregui, A.; Ablat, H.; Ruiz-Rubio, L.; López-Ortega, A.; Elliott, S. D.; Knez, M. Suppressing the Thermal and Ultraviolet Sensitivity of Kevlar by Infiltration and Hybridization with ZnO. *Chem. Mater.* **2017**, 29 (23), 10068–10074.
- (45) Jur, J. S.; Sweet, W. J.; Oldham, C. J.; Parsons, G. N. Atomic Layer Deposition of Conductive Coatings on Cotton, Paper, and Synthetic Fibers: Conductivity Analysis and Functional Chemical Sensing Using "All-Fiber" Capacitors. *Adv. Funct. Mater.* **2011**, *21* (11), 1993–2002.
- (46) Brozena, A. H.; Oldham, C. J.; Parsons, G. N. Atomic Layer Deposition on Polymer Fibers and Fabrics for Multifunctional and Electronic Textiles. *J. Vac. Sci. Technol., A* **2016**, 34 (1), No. 010801.
- (47) Mundy, J. Z.; Shafiefarhood, A.; Li, F.; Khan, S. A.; Parsons, G. N. Low Temperature Platinum Atomic Layer Deposition on Nylon-6 for Highly Conductive and Catalytic Fiber Mats. *J. Vac. Sci. Technol., A* **2016**, 34 (1), No. 01A152.
- (48) Sweet, W. J.; Jur, J. S.; Parsons, G. N. Bi-Layer Al2O3/ZnO Atomic Layer Deposition for Controllable Conductive Coatings on Polypropylene Nonwoven Fiber Mats. *J. Appl. Phys.* **2013**, *113* (19), 194303.
- (49) Senghor, F. D.; Wasselynck, G.; Bui, H. K.; Branchu, S.; Trichet, D.; Berthiau, G. Electrical Conductivity Tensor Modeling of Stratified Woven-Fabric Carbon Fiber Reinforced Polymer Composite Materials. *IEEE Trans. Magn.* **2017**, *53* (6), 1–4.
- (50) Lu, L.; Xing, D.; Xie, Y.; Teh, K. S.; Zhang, B.; Chen, S.; Tang, Y. Electrical Conductivity Investigation of a Nonwoven Fabric Composed of Carbon Fibers and Polypropylene/Polyethylene Core/Sheath Bicomponent Fibers. *Mater. Des.* **2016**, *112*, 383–391.
- (51) Chen, Y.; Ginga, N. J.; LePage, W. S.; Kazyak, E.; Gayle, A. J.; Wang, J.; Rodríguez, R. E.; Thouless, M. D.; Dasgupta, N. P. Enhanced Interfacial Toughness of Thermoplastic–Epoxy Interfaces Using ALD Surface Treatments. ACS Appl. Mater. Interfaces 2019, 11 (46), 43573–43580.
- (52) Wooding, J. P.; Li, Y.; Kalaitzidou, K.; Losego, M. D. Engineering the Interfacial Chemistry and Mechanical Properties of Cellulose-Reinforced Epoxy Composites Using Atomic Layer Deposition (ALD). *Cellulose* **2020**, 27 (11), 6275–6285.
- (53) Banerjee, P.; Lee, W.-J.; Bae, K.-R.; Lee, S. B.; Rubloff, G. W. Structural, Electrical, and Optical Properties of Atomic Layer Deposition Al-Doped ZnO Films. *J. Appl. Phys.* **2010**, *108* (4), No. 043504.
- (54) Dasgupta, N. P.; Neubert, S.; Lee, W.; Trejo, O.; Lee, J.-R.; Prinz, F. B. Atomic Layer Deposition of Al-Doped ZnO Films: Effect

- of Grain Orientation on Conductivity. Chem. Mater. 2010, 22 (16), 4769-4775.
- (55) Shah, M.; Chaudhary, V. Flow Modeling and Simulation Study of Vacuum Assisted Resin Transfer Molding (VARTM) Process: A Review. In *IOP Conference Series: Materials Science and Engineering*; Institute of Physics Publishing, 2020; Vol. 872, p 012087. DOI: 10.1088/1757-899X/872/1/012087.
- (56) Dasgupta, N. P.; Mack, J. F.; Langston, M. C.; Bousetta, A.; Prinz, F. B. Design of an Atomic Layer Deposition Reactor for Hydrogen Sulfide Compatibility. *Rev. Sci. Instrum.* **2010**, *81* (4), No. 044102.
- (57) Miccoli, I.; Edler, F.; Pfnür, H.; Tegenkamp, C. The 100th Anniversary of the Four-Point Probe Technique: The Role of Probe Geometries in Isotropic and Anisotropic Systems. *J. Phys.: Condens. Matter* **2015**, *27* (22), 223201.
- (58) Lord, J. D.; Roebuck, B.; Morrell, R.; Lube, T. 25 Year Perspective Aspects of Strain and Strength Measurement in Miniaturised Testing for Engineering Metals and Ceramics. *Mater. Sci. Technol.* **2010**, 26 (2), 127–148.
- (59) Bruno, L. Mechanical Characterization of Composite Materials by Optical Techniques: A Review. *Opt. Lasers Eng.* **2018**, *104*, 192–203
- (60) Sause, M. G. R. Digital Image Correlation. In *Springer Series in Materials Science*; Springer Verlag, 2016; Vol. 242, pp 57–129. DOI: 10.1007/978-3-319-30954-5\_3.
- (61) LePage, W. S.; Shaw, J. A.; Daly, S. H. Optimum Paint Sequence for Speckle Patterns in Digital Image Correlation. *Exp. Technol.* **2017**, *41* (5), 557–563.
- (62) Andrianov, I. V.; Danishevs'kyy, V. V.; Kalamkarov, A. L. Analysis of the Effective Conductivity of Composite Materials in the Entire Range of Volume Fractions of Inclusions up to the Percolation Threshold. *Composites, Part B* **2010**, *41* (6), 503–507.
- (63) Haghgoo, M.; Ansari, R.; Hassanzadeh-Aghdam, M. K. Prediction of Electrical Conductivity of Carbon Fiber-Carbon Nanotube-Reinforced Polymer Hybrid Composites. *Composites, Part B* **2019**, *167*, 728–735.
- (64) Pal, G.; Kumar, S. Multiscale Modeling of Effective Electrical Conductivity of Short Carbon Fiber-Carbon Nanotube-Polymer Matrix Hybrid Composites. *Mater. Des.* **2016**, *89*, 129–136.
- (65) Haj-Ali, R.; Zemer, H.; El-Hajjar, R.; Aboudi, J. Piezoresistive Fiber-Reinforced Composites: A Coupled Nonlinear Micromechanical—Microelectrical Modeling Approach. *Int. J. Solids Struct.* **2014**, *51* (2), 491–503.
- (66) Hu, M. S.; Thouless, M. D.; Evans, A. G. The Decohesion of Thin Films from Brittle Substrates. *Acta Metall.* **1988**, 36 (5), 1301–1307.
- (67) Thouless, M. D. Crack Spacing in Brittle Films on Elastic Substrates. J. Am. Ceram. Soc. 1990, 73 (7), 2144–2146.
- (68) Thouless, M. D.; Olsson, E.; Gupta, A. Cracking of Brittle Films on Elastic Substrates. *Acta Metall. Mater.* **1992**, 40 (6), 1287–1292.
- (69) Tapily, K.; Gu, D.; Baumgart, H.; Namkoong, G.; Stegall, D.; Elmustafa, A. A. Mechanical and Structural Characterization of Atomic Layer Deposition-Based ZnO Films. *Semicond. Sci. Technol.* **2011**, 26 (11), 115005–115012.